Radial-Flux Rotational Wireless Power Transfer System With Rotor State Identification

Longyang Wang, Jiangui Li, Huiying Chen, and Zijun Pan

***Abstract*—A radial-flux rotational wireless power transfer (RF-R-WPT) system with rotor state identification function has been proposed to provide power to the devices mounted on a rotating shaft in this article. It can not only transmit electric power from the stationary side to the rotating side but also monitor the rotor state at the same time, improving the stability, security, and service life of the traditional brushes and slip rings. First, the topology and operation principle of the RF-R-WPT system have been proposed. Second, the radial-flux coupler has been designed and optimized. Third, the rotor state identification algorithm has been proposed. Fourth, the voltage and current variation of the primary side and the secondary side of the S–S compensation topology and LCC-S compensation topology have been studied separately, while the coupling degree of the coupler changes. A mutual inductance identification model has been proposed. Fifth, a prototype has been built and tested. From the experimental results, it is verified that the system can realize the power transmission of 13.5 W with a comprehensive efficiency of 74.1% and measure the rotor speed stably to determine its state at the same time.**

***Index Terms*—Efficiency, mutual inductance, rotational wireless power transfer system, state identification.**

I. INTRODUCTION

ROTATIONAL electrical equipment is widely used in industry these days [1]–[3]. At present, brush and slip ring is one of the main electric power transmission equipment for rotating loads. However, the contact of the slip ring and the bushes may cause electric spark, leading to accident in some cases [4]. In addition, the contact surface of the slip ring might be worn out for long-term work, increasing the contact resistance. Eventually, it leads to poor contact between the brush and the slip ring [5]. These problems greatly reduce the service life of the brushes and slip rings and also reduce the reliability of the power supply of the rotating equipment.

To solve the problems of poor safety and stability caused by traditional contact electric power supply, rotary transformer is proposed and used for power transmitting [6], [7]. The overall reliability and lifetime have been improved because of the application of the rotary transformer. However, its low-frequency characteristics make it necessary to have a small working air gap, which is usually only 1 mm or less. This limits its application in the cases involving large vibration and shock.

The magnetic coupling resonance wireless power transfer (MCR-WPT) technology, in which the electric power is contactless transmitted based on the resonance of the coupler, was proposed. It played important roles in areas, such as robots [8], unmanned aerial vehicles [9], electric vehicles [10], and power grid monitoring equipment [11] because of its long transmitting distance, noncontact characteristics, high security, and high reliability. The application of wireless power transfer technology in rotating equipment has also been proposed as a substitute of brushes and slip rings, greatly improving the stability of rotational equipment and reducing equipment maintenance costs. Different from the rotary transformer, rotational wireless power transfer (R-WPT) system works at a much higher frequency (usually 20 kHz–5 MHz), and it can transmit power with a larger gap (1 cm or more) between the transmitting and receiving part while maintaining a high transmitting efficiency. In recent years, R-WPT technology has attracted more and more attention of scholars [12]–[14].

Song *et al.* [12] designed an R-WPT system for the solar wing driving of the spacecraft. It is characterized by high efficiency, safety, and flexibility. However, large volume and low integration limit its development. Lee and Ahn [13] presented an R-WPT system for powering diagnostic sensors on a rotating spindle. The receiving coil had been installed on the spindle at 30-cm interval, which picks up electric energy and supply power to the sensors, and the transmitting coil was fixed on the side bracket. But its stability, integration, and transmission power need to be improved. Sofia *et al.* [14] proposed an R-WPT device for biological centrifuges, of which uninterrupted work is often needed and the sensors, such as temperature and humidity, are also needed to be powered. Higher efficiency R-WPT system with extended function are preferable to its promotion and application.

In this article, a radial-flux rotational wireless power transfer (RF-R-WPT) system with rotor state identification function has been proposed in order to supply electric power to the devices mounted on the rotating shaft. It can transmit energy and monitor the rotor state at the same time. First, the structural topology and working principle of the RF-R-WPT system have been analyzed. Second, a radial-flux coupler has been proposed, and the characteristic of mutual inductance during its rotation has been studied. The radial-flux coupler and its magnetic shielding pad have been optimized, respectively, considering the coupling coefficient and

---

Manuscript received July 29, 2021; revised November 4, 2021; accepted November 27, 2021. Date of publication December 6, 2021; date of current version January 19, 2022. Recommended for publication by Associate Editor M. Vitelli. *(Corresponding author: Jiangui Li.)*

The authors are with the School of Mechanical and Electronic Engineering, Wuhan University of Technology, Hubei 430070, China (e-mail: wanglongyang1994@163.com; jianguili@whut.edu.cn; 1105694861@qq.com; panzijun1186772136@foxmail.com).

Color versions of one or more figures in this article are available at https://doi.org/10.1109/TPEL.2021.3132702.

Digital Object Identifier 10.1109/TPEL.2021.3132702

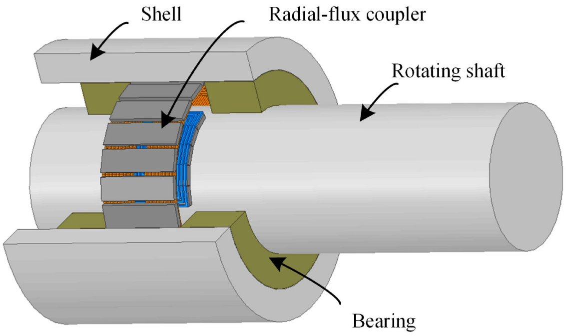

Fig. 1. 3-D schematic diagram of RF-R-WPT system.

magnetic shielding ability. Third, a state identification algorithm based on the RF-R-WPT system has been proposed. Fourth, the voltage and current characteristics based on the S-S and LCC-S compensation topologies have been studied separately with the degree of coupling changing. The mutual inductance identification models based on the LCC-S compensation topology have been proposed. Fifth, the RF-R-WPT system experimental platform with state identification function has been built, and the input and output characteristics of the RF-R-WPT system at constant rotor speed and locked rotor state have been studied separately.

II. TOPOLOGY AND PRINCIPLE

The purpose of the proposed RF-R-WPT system is to supply electric power to the devices on the rotating shaft. The overall power required is 13 W. The system can monitor the rotational speed of the rotor, and warning is given when the rotating shaft is locked. The 3-D schematic diagram of the proposed RF-R-WPT system is shown in Fig. 1. There are mainly three parts, the transmitting coils, receiving coils, and the power electronic circuits. The transmitting coils and receiving coils together are referred as radial-flux coupler in this article. The dc voltage source, high frequency inverter, current acquisition circuit, and primary compensation circuit are mounted on the shell (not shown in Fig. 1). The secondary side compensation circuit, rectifier, wave filter, and current acquisition circuit are embedded in a box, which is mounted on the rotating shaft with rubber vibration isolation (not shown in Fig. 1).

The system topology and principle are shown in Fig. 2. On the stationary side (primary side) of the RF-R-WPT system, the measuring sensor is introduced between the dc power supply and the inverter, to monitor the output current I_{DC} of the dc power supply. On the rotating side (secondary side), the measuring sensor is connected between the filter and the voltage regulator, to monitor the output voltage U_{WF} and output current I_{WF} of the filter. For the measuring sensor on the rotating side, connecting it after the filter C_{WF} can effectively reduce the sampling frequency required and improve the sampling accuracy. The high-frequency components of the voltage and current of the rotating side will be filtered out by the filter C_{WF}, and only the low-frequency components related to the change of mutual inductance are retained. It should be noted that the filter capacitor C_{WF} cannot be too large, otherwise the low-frequency components of the voltage and current will also be filtered out, which will result in the inability to measure the current and voltage changes.

The receiving coil of the radial-flux coupler (proposed and optimized in Sections III and IV) rotates with the shaft. The mutual inductance of the coupler changes with the rotation angle of the shaft. Therefore, the rotor state can be obtained by state recognition algorithm (proposed in Section V), according to the actual mutual inductance. The variation of mutual inductance will cause the change of input current I_{DC} and output voltage U_{WF} and current I_{WF} of the RF-R-WPT system. Based on the input current and output voltage and current, the real time mutual inductance is obtained by the mutual inductance identification model (proposed in Section VI).

III. RADIAL FLUX COUPLER

Mutual inductance is one of the key factors affecting the transmission performance of WPT systems. Improving mutual inductance within a certain range can improve system transmission efficiency and reduce power loss [15]–[18]. For the radial-flux coupler, the mutual inductance changes with the rotation of the receiving coil.

The radial-flux coupler proposed in this article is composed of four coils, namely, two transmitting coils and two receiving coils, as shown in Fig. 3. The two transmitting coils are wound on the inner surface of the shell (each coil taking up half of the area), and the receiving coils are wound on the outer surface of the shaft. The transmitting coils and the receiving coils are connected in series, respectively. The transmitting coils and receiving coils are mounted coaxially, as shown in Fig. 4. The diameter of the transmitting coils is 100 mm (limited by the inner diameter of the shell), and the diameter of the receiving coils is 80 mm (limited by the outer diameter of the shaft). The distance between the transmitting coil and the receiving coil is 1 cm, which can avoid the collision damage caused by shaft vibration and improve the reliability of the system.

The copper core of the litz wire used has a circular cross-section with a diameter of 1 mm and a cross-sectional area of 0.785 mm^2. The litz wire consists of 600 copper wires (0.04 mm in diameter of a single copper wire) to avoid skin effect. The litz wire is characterized by excellent heat resistance, it can withstand 155 °C high temperature.

It is known from the above sections that the size of the radial-flux coupler is restricted by the installation environment, especially for the transmitting coils. In the design, to obtain greater transmission power, the transmitting coils are designed as large as possible. The parameters of the transmitting coils are given in Table I.

Given the parameters of the transmitting coils, the receiving coils can be optimized to obtain the best coupling performance by finite-element method (in static magnetic field). The length l_R and high h_R of the receiving coils have greater influence on the coupling degree of the coupler than other parameters. Therefore, the relationship between the length l_R and height h_R of the receiving coils and the coupling degree of the coupler has been studied through the finite-element method. It is important to note that the coupling degree of the radial-flux coupler varies

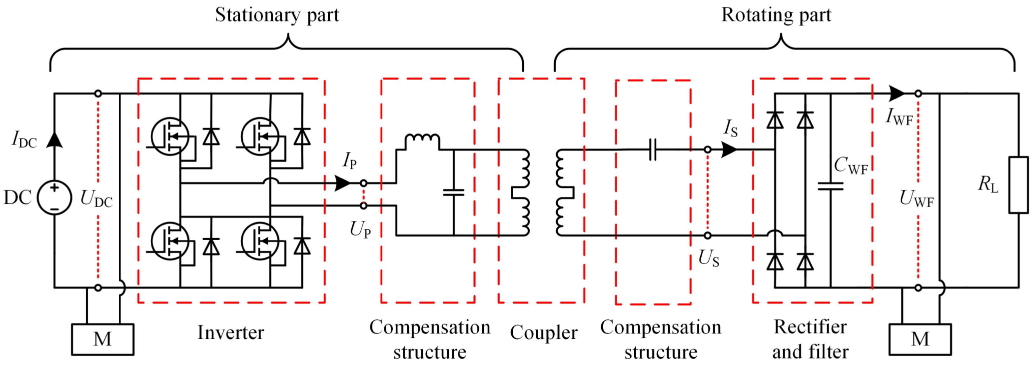

Fig. 2. RF-R-WPT system topology and principle (“M” is the measuring sensor used to measure current and voltage; C_{WF} is the filter capacitor; R_{L} is the load; I_{DC} and U_{DC} are the output current and voltage of the dc power supply, respectively; I_{DC} is the pulsed current; I_P and U_P are the output current and voltage of the inverter, respectively; I_S and U_S are the input current and voltage of the rectifier, respectively; and I_{WF} and U_{WF} are the output current and voltage of the filter, respectively).

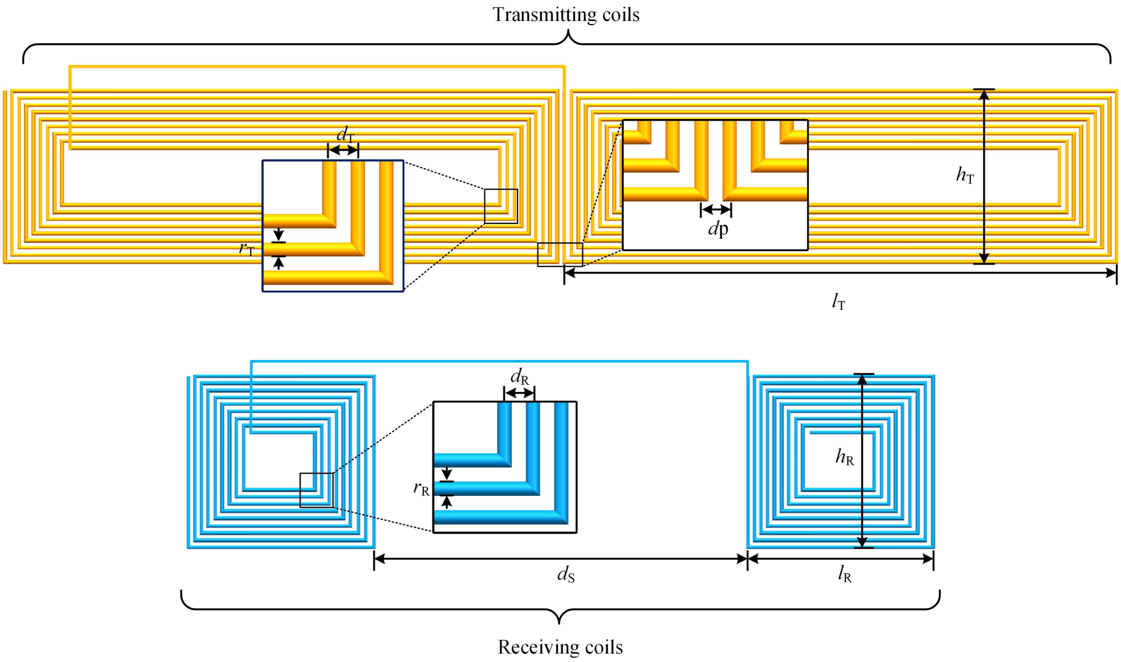

Fig. 3. Expansion view of radial flux coupler (r_T, d_T are the diameter and line spacing of the litz wire used in the transmitting coils respectively; l_T, h_T, and n_T are the length, height, and number of turns of a single transmitting coil, respectively; d_P is the distance between the two transmitting coils; r_R, d_R is the diameter and line spacing of the litz wire used in the receiving coils; l_R, h_R, and n_R are the length, height, and number of turns of a single receiving coil; and d_S is the distance between the two receiving coils).

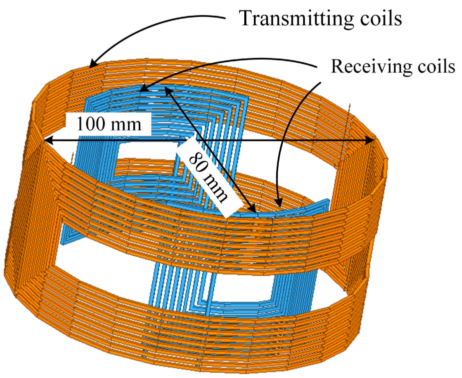

Fig. 4. Schematic diagram of radial-flux coupler.

TABLE I
PARAMETERS OF TRANSMITTING COILS

Symbol	Description	Value
r_T	Litz wire diameter	1 mm
d_T	Wire spacing	2 mm
l_T	Coil length	155 mm
h_T	Coil height	48 mm
d_P	The distance between coils	2 mm
n_T	Coil turns	9

with the rotation angle α. Furthermore, the relative position of the transmitting coils and the receiving coils changes with the rotation angle α of the rotor. Therefore, the rotation angle α should be taken into consideration during optimization design.

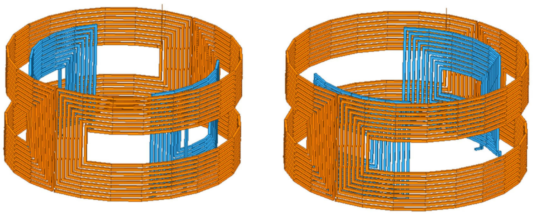

0°, 180°, 360°
(a)

90°, 270°
(b)

Fig. 5. Schematic diagram of rotation angle α. (a) At $\alpha = 0°$, 180°, and 360°. (b) At $\alpha = 90°$ and 270°.

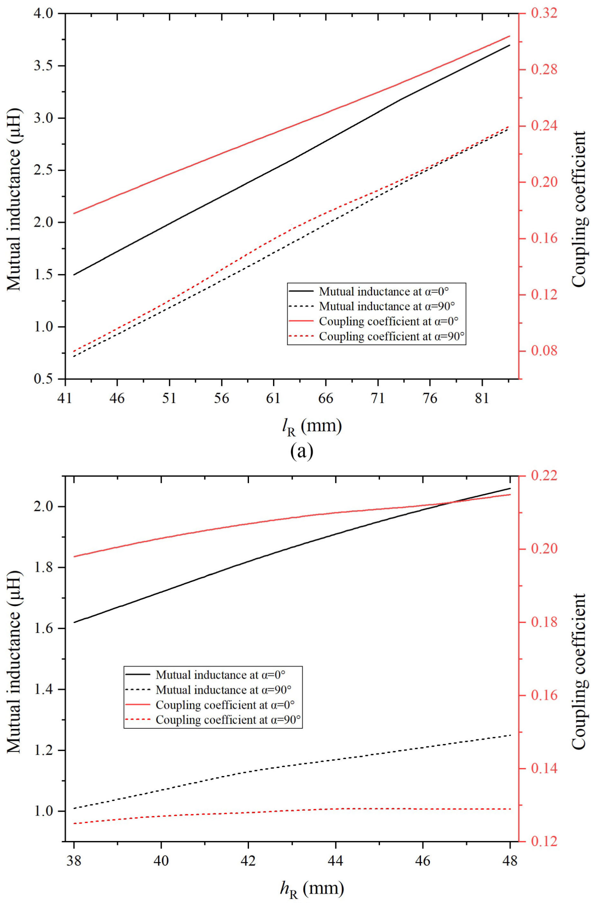

(a)

(b)

Fig. 6. Mutual inductance and coupling coefficient with different parameters. (a) With l_R changing. (b) With h_R changing.

The maximum (at $\alpha = 0°$, 180°, and 360°) and minimum (at $\alpha = 90°$ and 270°) coupling degree are shown in Fig. 5(a) and (b), respectively. To simplify the design, the receiving coils have been optimized at $\alpha = 0°$ and $\alpha = 90°$.

At $\alpha = 0°$ and 90°, the mutual inductance and coupling coefficient of the coupler versus the length L_R of the receiving coils is shown in Fig. 6(a) at $h_R = 48$ mm. It can be clearly seen that the mutual inductance and coupling coefficient of the coupler are proportional to L_R.

At $\alpha = 0°$ and 90°, the mutual inductance and coupling coefficient of the coupler versus the high h_R of the receiving coil is shown in Fig. 6(b) at $L_R = 53$ mm. It can be known that the increase of h_R contributes to the increase of mutual inductance and coupling coefficient of the coupler. Specially, the increase in h_R has a greater impact on the coupling coefficient of the coupler at $\alpha = 0°$, than that of $\alpha = 90°$.

TABLE II
PARAMETERS OF RECEIVING COILS

Symbol	Description	Value
r_{R}	Litz wire diameter	1 mm
d_{R}	Wire spacing	2 mm
l_{R}	Coil length	53 mm
h_{R}	Coil height	48 mm
d_{S}	Distance between coils	72 mm
n_{R}	Coil turns	9

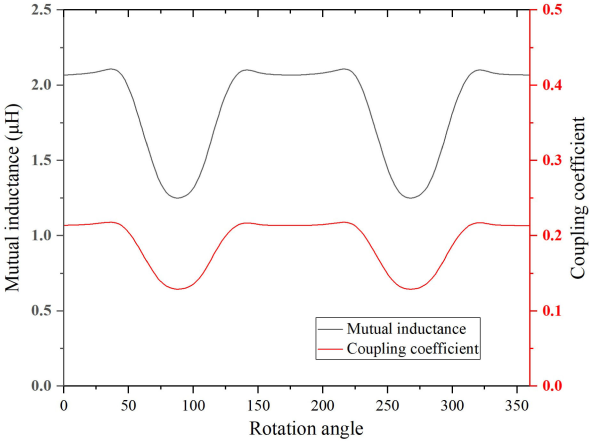

Fig. 7. Mutual inductance and coupling coefficient with rotation angle changing.

The coupling coefficient is generally in the range to 0.1–0.5 according to the specific design [19]–[22]. Considering the power, efficiency, and frequency splitting, the coupling coefficient of the coupler (with ferrite) selected in this article is 0.28 at the rotation angle of 0°. The coupling coefficient of the radial-flux coupler without ferrite selected in this article is 0.21. The parameters of the receiving coils have been determined, as listed in Table II. At $\alpha = 0°$, the mutual inductance and the coupling coefficient of the radial-flux coupler without ferrite is 2.06 μH and 0.21, respectively; at $\alpha = 90°$, the mutual inductance and the coupling coefficient of the coupler without ferrite is 1.25 μH and 0.13, respectively.

Finally, the mutual inductance and coupling coefficient of the radial-flux coupler proposed in this article with the rotation angle α changing is shown in Fig. 7. It can be known that the mutual inductance value of the radial-flux coupler reaches the minimum value at $\alpha = 90°$ and 270°, which is 1.25 μH. At $\alpha = 0°$, 180°, and 360°, the mutual inductance is 2.06 μH. At $\alpha = 60°$, the mutual inductance is 1.72 μH. The mutual inductance changes twice in one rotation period.

IV. OPTIMIZATION DESIGN OF MAGNETIC SHIELDING PAD

Ferrite pad is added to the WPT system to improve the coupling degree and reduce the leakage flux [23]–[25]. In this section, the magnetic shielding pad of radial-flux coupler has been optimized, considering the coupling degree, magnetic field

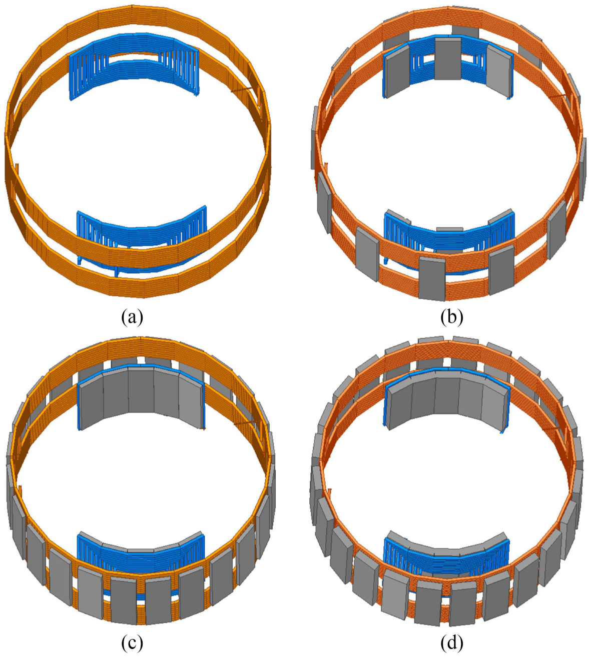
(a) (b) (c) (d)

Fig. 8. Radial-flux couplers with different magnetic shielding mechanisms. (a) No ferrite pad. (b) Ferrite pad B. (c) Ferrite pad C. (d) Ferrite pad D.

TABLE III
MATERIAL PROPERTY PARAMETERS OF FERRITE

Contents	Values
Relative permeability	1000
Bulk conductivity	0.01 S/m
Young's modulus	11900 kN/cm^2

TABLE IV
SIZES OF DIFFERENT FERRITE PAD

Types	Length	Width	Height	Quantity
B	42 mm	10 mm	1.5 mm	12
C	42 mm	10 mm	1.5 mm	24
D	42 mm	10 mm	3 mm	24

distribution, and eddy current field distribution. The radial-flux coupler without ferrite pad and with ferrite pad B, C, and D have been designed, as shown in Fig. 8(a)–(d), separately. The material property parameters of ferrite are given in Table III. The sizes of ferrite pad B, ferrite pad C, and ferrite pad D are shown in Table IV.

The finite-element method has been adopted and the simulated magnetic field distribution, eddy current field distribution, mutual inductance, and coupling coefficient of the radial-flux coupler with the above-mentioned four kinds of ferrite pad have been obtained at $\alpha = 0°$. The magnetic field distribution (which is obtained by static magnetic field simulation analysis, and the simulation current is 1 A) is shown in Fig. 9, the eddy current field distribution (which is obtained by eddy current field simulation analysis, and the simulation current and frequency are 1 A and 300 kHz) is shown in Fig. 10, and the mutual inductance and coupling coefficient (which is obtained by static magnetic field simulation analysis, and the simulation current is 1 A) of the radial-flux coupler are shown in Fig. 11.

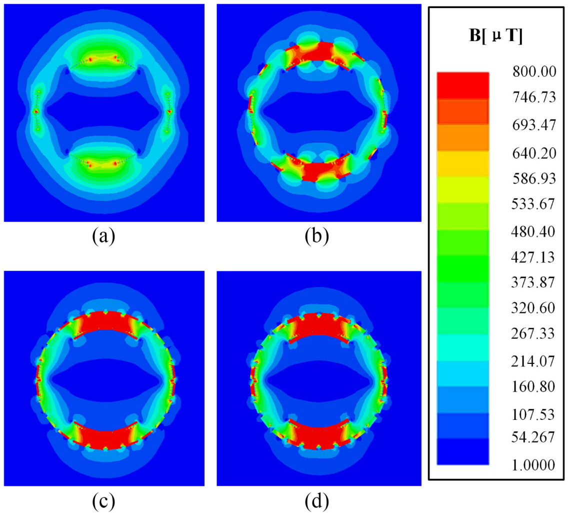

(a) (b) (c) (d)

Fig. 9. Magnetic field distribution of the coupler under different ferrite pads. (a) No ferrite pad. (b) Ferrite pad B. (c) Ferrite pad C. (d) Ferrite pad D.

It can be known from Fig. 9 that comparing with the radial-flux coupler without ferrite pad, ferrite pad B can effectively weaken the magnetic field around the radial-flux coupler. In addition, with the increase of ferrite, pad C is better than B for magnetic shielding ability, but pad D is similar to that of C. In summary, the increase of ferrite leads to better magnetic shielding ability. But after the ferrite reaches a certain amount, adding ferrite alone has little effect on the magnetic shielding ability.

As shown in Fig. 10, the eddy current on ferrite pad B is the smallest and that on ferrite pad D is the largest. The eddy current increases with the increase of ferrite number and volume. This will lead to greater energy loss. Therefore, considering the eddy current effect, the number and volume of ferrite should also be limited.

It can be recognized from Fig. 11 that the radial-flux coupler with ferrite pad B is provided with larger mutual inductance and coupling coefficient than that of the radial-flux coupler without ferrite pad. Ferrite pad C is better than B in terms of mutual inductance and coupling coefficient improvement. However, comparing with C, the ferrite pad D does not significantly improve the mutual inductance and coupling coefficient.

Comprehensive consideration of magnetic shielding, eddy current field, mutual inductance, and coupling coefficient, the radial-flux coupler with ferrite pad C is chosen in this article. Finally, the self-inductance and resistance of the transmitting coil with ferrite are 29.6 μH and 0.189 Ω, respectively. The self-inductance and resistance of the receiving coil with ferrite are 8.2 μH and 0.047 Ω, respectively. The above results are obtained by finite element simulation.

V. STATE IDENTIFICATION ALGORITHM

The state identification algorithm has been proposed in this article, as shown in Fig. 12. The identification algorithm is as follows.

1) First, under the optimal load and voltage (introduced in Section VII), the primary side current of the RF-R-WPT

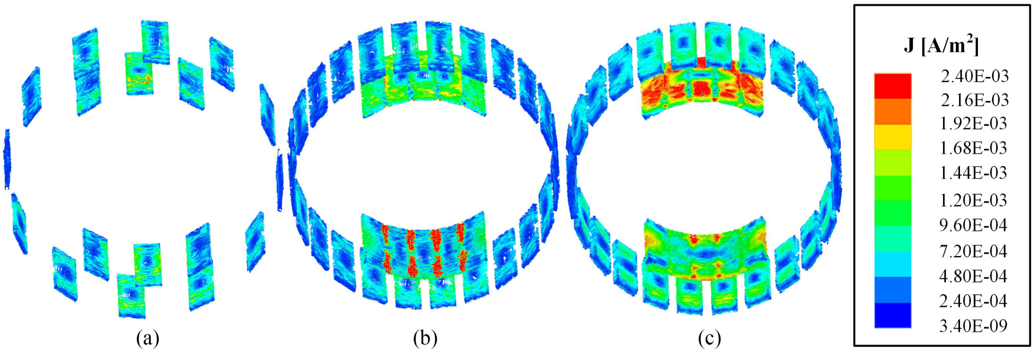

Fig. 10. Eddy current field distribution of different ferrite pads. (a) Ferrite pad B. (b) Ferrite pad C. (c) Ferrite pad D.

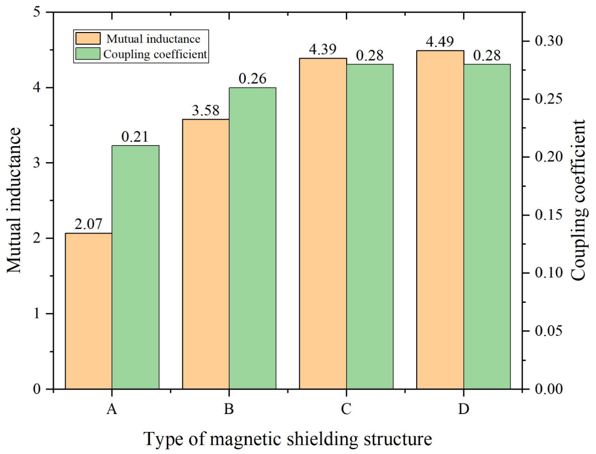

Fig. 11. Mutual inductance and coupling coefficient of radial-flux coupler under different ferrite pads.

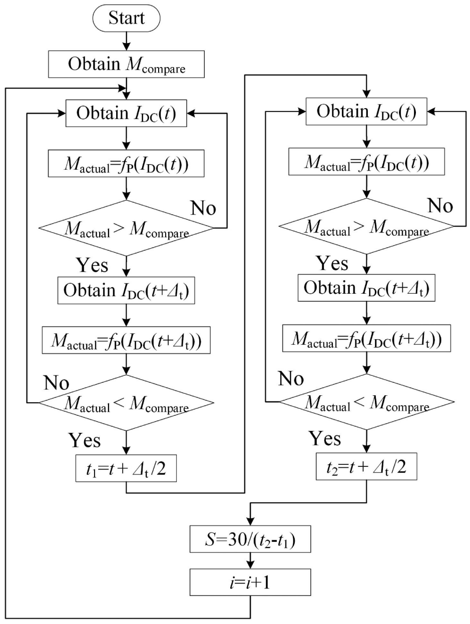

Fig. 12. State identification algorithm (M_{compare} is the mutual inductance value obtained through the mutual inductance identification model at $\alpha = 60°$; $f_P(x)$ is the mutual inductance identification model based on $I_{\text{DC}}(t)$; t is the time variable; $I_{\text{DC}}(t)$ is the current collected at time t; Δt is the sampling time interval; and S is the speed signal (r/min)).

system is obtained by the measuring sensor, at $\alpha = 60°$. According to this current, M_{compare} is obtained by the mutual inductance identification model (proposed in Section VI), and is set as a comparison (It can be seen from Fig. 7 that at $\alpha = 60°$, the mutual inductance value of the radial-flux coupler is between 0° and 90°. Using the above-mentioned mutual inductance as a comparison can avoid misjudgment caused by mutual inductance identification model error).

2) According to the real-time current $I_{\text{DC}}(t)$ of primary side, the corresponding mutual inductance M_{actual} is calculated by the mutual inductance identification model $f_P(x)$.
3) Comparing M_{compare} with M_{actual}, if $M_{\text{actual}} < M_{\text{compare}}$, repeat Step2 and continue acquire $I_{\text{DC}}(t)$ and M_{actual} until $M_{\text{actual}} > M_{\text{compare}}$, thus the variant t is obtained.
4) With $M_{\text{actual}} > M_{\text{compare},}$ the current of the primary side at the next sampling interval $I_{\text{DC}}(t + \Delta t)$ is obtained. The mutual inductance at this time is calculated by $f_{\text{P}}(I_{\text{DC}}(t + \Delta t))$.
5) Comparing M_{compare} with M_{actual}, if $M_{\text{actual}} > M_{\text{compare}}$, repeat Step2 and continue obtaining $I_{\text{DC}}(t)$ and M_{actual} until both conditions are met. Thus, the variant t is obtained, and $t_1 = t + \Delta t/2$.
6) Repeat the above steps to get the next time t_2 that meets the conditions.
7) The rotor speed is obtained by $S = 30/(t_2 - t_1)$.
8) The initial value of i is 1, and each time the program is executed, i is incremented by 1. When i remains unchanged for a long time, it can be known that the rotor is locked. At a constant speed, the increase of i within one minute is twice that of S. This can be used to monitor the speed S for errors.

It should be noted that there are three types of mutual inductance identification models, namely $f_P(x)$, $f_{\text{SC}}(x)$, and $f_{\text{SV}}(x)$. The corresponding inputs of the above three mutual inductance identification models are I_{DC}, I_{WF}, and U_{WF}, respectively. Different models correspond to different functions. According to $f_P(x)$, the rotor state can be identified on the stationary (primary) side. According to $f_{\text{SC}}(x)$ or $f_{\text{SV}}(x)$, the rotor state can be identified on the rotating (secondary) side. For the state recognition algorithm, the three mutual inductance identification models can substitute with each other, according to actual applications.

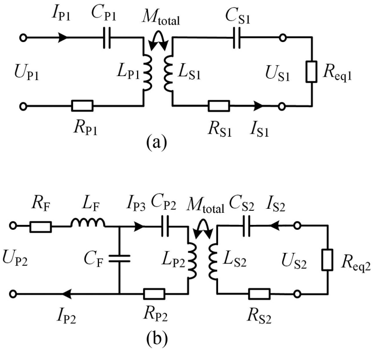

Fig. 13. Equivalent circuit diagram of WPT system based on different compensation topologies (U_{P1}, U_{P2}, U_{S1}, U_{S2}, R_{eq1}, and R_{eq2} are the input, output voltage, and equivalent load of the two systems, respectively; $L_{P1}, L_{S1}, R_{P1}, R_{S1}, C_{P1}, C_{S1}, I_{P1}$, and I_{S1} are the self-inductance, parasitic resistance, compensation capacitance, and current of the RF-R-WPT system based on the S–S compensation structure; and $L_{P2}, L_F, L_{S2}, R_{P2}, R_F, R_{S2}, C_{P2}, C_F, C_{S2}, I_{P2}$, and I_{S2} are the self-inductance, parasitic resistance, compensation capacitance, and current of the RF-R-WPT system based on the LCC-S compensation structure). (a) S-S. (b) LCC-S.

VI. COMPENSATION TOPOLOGY AND MUTUAL INDUCTANCE IDENTIFICATION MODEL

The previous section introduced the RF-R-WPT system topology and state identification algorithm. This section focuses on the compensation topology and mutual inductance identification model. Compensation topologies can effectively improve the power factor and reduce energy loss. Currently, the commonly used compensation topologies are mainly S-S and LCC-S. The input and output characteristics of the WPT system based on the aforementioned two compensation topologies have been analyzed separately, to find a compensation topology suitable for the frequent variation of mutual inductance.

The transmitting coils and the receiving coils of the radial-flux coupler are consisting of two serial coils in series, respectively. For convenience, the mutual inductance between the transmitting coils and the receiving coils is equivalent to M_{total}. It is assumed that the dc power, rectifier, and inverter used are ideal components. Based on the fundamental component of square wave, the WPT circuit is analyzed [26]. The equivalent circuit diagrams of the WPT system based on the S–S and LCC-S compensation topologies are shown in Fig. 13(a) and (b), respectively.

For the RF-R-WPT system with S–S compensation topology, according to Kirchhoff's voltage theorem (KVL), the following equation can be obtained:

$$\begin{cases} U_{P1} = I_{P1}\left(j\omega L_{P1} + \frac{1}{j\omega C_{P1}} + R_{P1}\right) + j\omega M_{\text{total}} I_{S1} \\ -R_{\text{eq1}} I_{S1} = j\omega M_{\text{total}} I_{P1} + I_{S1}\left(j\omega L_{S1} + \frac{1}{j\omega C_{S1}} + R_{S1}\right). \end{cases} \tag{1}$$

When $j\omega L_{P1} + 1/j\omega\, C_{P1} = 0, j\omega L_{S1} + 1/j\omega\, C_{S1} = 0$, in the case of ignoring R_{P1} and R_{S1}, the following equation can be obtained as follows:

$$\begin{cases} I_{P1} = \frac{U_{P1} R_{\text{eq1}}}{\omega^2 {M_{\text{total}}}^2} \\ I_{S1} = \frac{U_{P1}}{j\omega M_{\text{total}}} \\ U_{S1} = \frac{U_{P1} R_{\text{eq1}}}{j\omega M_{\text{total}}}. \end{cases} \tag{2}$$

For the WPT system with LCC-S compensation topology, according to KVL, the following equation can be obtained as follows:

$$\begin{cases} U_{P2} = I_{P2}(j\omega L_F + R_F) + (I_{P2} - I_{P3})\frac{1}{j\omega C_F} \\ (I_{P2} - I_{P3})\frac{1}{j\omega C_F} = I_{P3}(j\omega L_{P2} + \frac{1}{j\omega C_{P2}} + R_{P2}) \\ \quad + j\omega M_{\text{total}} I_{S2} \\ -R_{\text{eq2}} I_{S2} = j\omega M_{\text{total}} I_{P3} + I_{S2}(j\omega L_{S2} + \frac{1}{j\omega C_{S2}} + R_{S2}). \end{cases} \tag{3}$$

When $j\omega L_F + 1/j\omega\, C_F = 0$, $j\omega(L_{P2} - L_F) + 1/j\omega\, C_{P2} = 0$, $j\omega L_{S2} + 1/j\omega\, C_{S2} = 0$, in the case of ignoring R_F, R_{P2}, and R_{S2}, the following equation can be obtained as follows:

$$\begin{cases} I_{P2} = \frac{{M_{\text{total}}}^2 U_{P2}}{{L_F}^2 R_{\text{eq2}}} \\ I_{S2} = \frac{M_{\text{total}} U_{P2}}{L_F R_{\text{eq2}}} \\ U_{S2} = \frac{M_{\text{total}} U_{P2}}{L_F}. \end{cases} \tag{4}$$

From (2), it can be found that for the S–S topology, the effective values of I_{P1}, I_{S1}, U_{S1} are in inverse proportion either to M_{total} or ${M_{\text{total}}}^2$, respectively. Therefore, with M_{total} decreasing, I_{P1}, I_{S1}, and U_{S1} will increase accordingly. This will increase the loss and the current and voltage stress of the components, which is not suitable for the condition of mutual inductance changing frequently. From (4), it can be found that for the LCC-S structure, the effective values of I_{P2}, I_{S2}, U_{S2} are proportional either to M_{total} or ${M_{\text{total}}}^2$, respectively. Therefore, as M_{total} drops, I_{P1}, I_{S1}, U_{S2} will experience different degrees of decline. Although it will not increase the current and voltage stress of the components, it will sacrifice a certain amount of transmission power.

Comprehensively, the LCC-S compensation topology has been selected as the compensation topology of the RF-R-WPT system in this article. To simplify the analysis, it has been assumed that the components used are ideal components. Then for the WPT system based on LCC-S compensation topology, $I_{P2} = I_{\text{DC}}$, $U_{S2} = U_{\text{WF}}$, $I_{S2} = I_{\text{WF}}$. The identification model of mutual inductance is shown as follows:

$$\begin{cases} f_P(x) = \sqrt{\frac{x {L_F}^2 R_{\text{eq2}}}{U_{P2}}}, x = I_{\text{DC}} \\ f_{\text{SC}}(x) = \frac{x L_F R_{\text{eq2}}}{U_{P2}}, x = I_{\text{WF}} \\ f_{\text{SV}}(x) = \frac{x L_F}{U_{P2}}, x = U_{\text{WF}}. \end{cases} \tag{5}$$

The inverter and rectifier are assumed to be ideal components. Ignoring R_F, the transmission efficiency η and transmission power P_{OUT} of the RF-R-WPT system based on the LCC-S compensation topology can be obtained as follows:

$$\begin{cases} P_{\text{OUT}} = \frac{{M_{\text{total}}}^2 R_{\text{eq2}} {U_{P2}}^2}{(R_{S2}+R_{\text{eq2}})^2 {L_F}^2} \\ \eta = \frac{R_{\text{eq2}}}{(R_{S2}+R_{\text{eq2}})(1+\frac{R_{P2}R_{S2}+R_{P2}R_{\text{eq2}}}{\omega^2 {M_{\text{total}}}^2})}. \end{cases} \tag{6}$$

VII. EXPERIMENTS AND ANALYSIS

To verify the theory proposed in this article, the RF-R-WPT system experimental platform has been built, as shown in Fig. 14. The values of the inductance, capacitance and resistance of the primary and the secondary are given in Table V. The full bridge

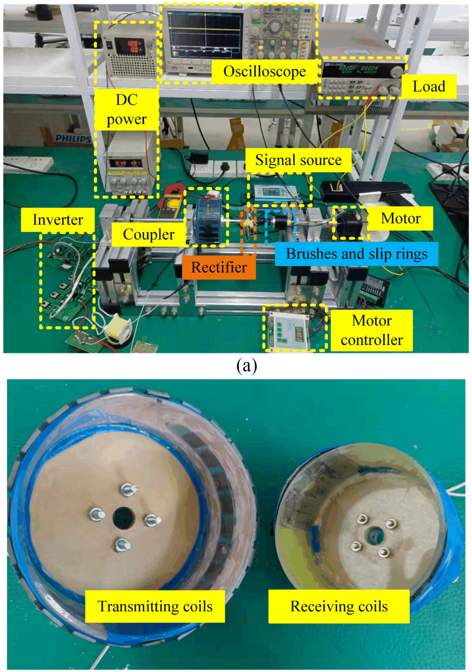

(a)

(b)

Fig. 14. RF-R-WPT system experimental platform. (a) Rotating experimental platform. (b) Radial flux coupler.

TABLE V
PROTOTYPE PARAMETERS

Description	Symbol	Value
Transmitting coils self-inductance	L_{P2}	27.5 μH
Receiving coils self-inductance	L_{S2}	8.6 μH
Transmitting coils resistance	R_{P2}	0.181 ohm
Receiving coils resistance	R_{S2}	0.045 ohm
Primary compensation inductance	L_F	2.82 μH
Primary compensation capacitor	C_{P2}	11398 pF
Primary compensation capacitor	C_F	99824 pF
Secondary compensation capacitor	C_{S2}	32718 pF
Filter capacitor	C_{WF}	400 μF
Frequency	K	300 kHz

inverter was used to generate square wave voltage and the full bridge rectifier is used to obtain stable output. The full bridge inverter is mainly composed of two IR2110s and four MOSFETs (C2M0080120). The full bridge rectifier is mainly composed of four diodes (DSEI30-06A).

The mutual inductance and the coupling coefficient of the radial-flux coupler versus the rotation angle α is obtained through measurement and simulation, as shown in Fig. 15. It can be seen from Fig. 15 that the rotor angle α is closely related to the mutual inductance. When the rotor rotates 360°, the mutual inductance goes through two cycles. It can also be seen that the mutual inductance of the radial-flux coupler approach maximum at $\alpha = 0°$, 180°, and 360°, which is 4.2 μH; at $\alpha = 90°$ and 270°, the mutual inductance reaches to the bottom value, which is 2.07 μH. The error of coupling coefficient is 2.3% at $\alpha = 0°$, and the error of mutual inductance is 2.9% at $\alpha = 0°$. The deviation is mainly caused by model manufacturing error and measurement error. The change trend of mutual inductance and coupling coefficient is similar.

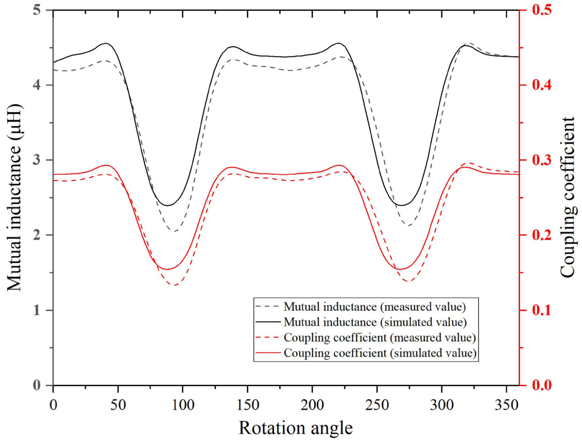

Fig. 15. Mutual inductance and coupling coefficient with rotation angle α changing.

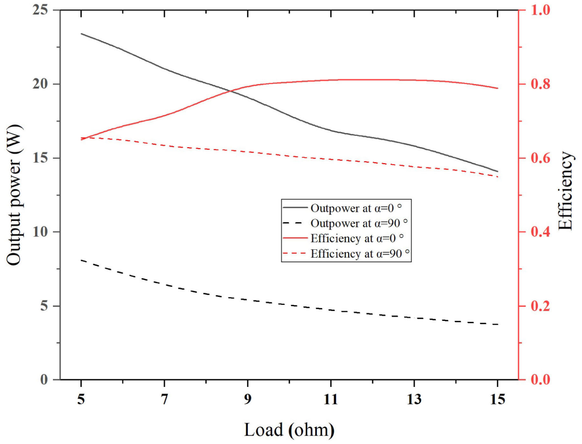

Fig. 16. Output power and efficiency with load changing.

To obtain the optimal working load, the output power and efficiency versus the load is obtained at $\alpha = 0°$ and 90°, respectively, at $U_{DC} = 12$ V, as shown in Fig. 16.

It can be known that at $\alpha = 0°$, as the load increases, the transmission efficiency first increases and then remains unchanged, but the output power gradually decreases. The efficiency reaches top when the load is 12 Ω. At $\alpha = 90°$, with the load increasing, the transmission efficiency and power both decreases. Because the RF-R-WPT system mainly works with a relatively high degree of coupling, the final load has been selected as 12 Ω in this article.

In addition, the relationship between the input voltage U_{DC} and the output power and efficiency at $\alpha = 0°$ and 90° under the optimal load has been studied, separately, as shown in Fig. 17. It can be known that as the input voltage U_{DC} increases, the output power of the two parameters both increase to different extents, the efficiency of the two also rises and then stabilizes. Both efficiencies reach their maximum value when the input voltage is 12 V.

Furthermore, the fluctuation of the input current I_{DC}, output voltage U_{WF} and output current I_{WF} of the RF-R-WPT system with rotation angle α changing has been obtained by measurement, respectively, at the input voltage is 12 V and the load is

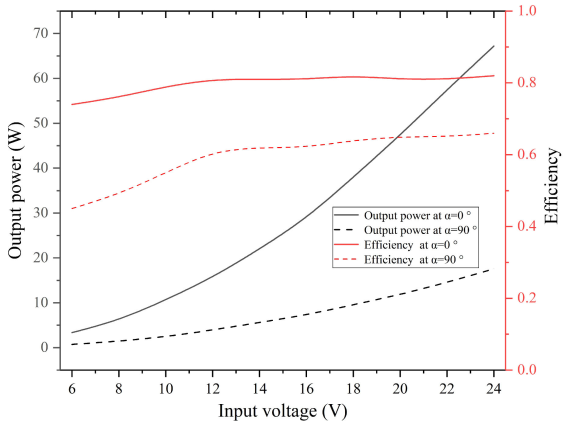

Fig. 17. Output power and efficiency with input voltage U_{DC} changing.

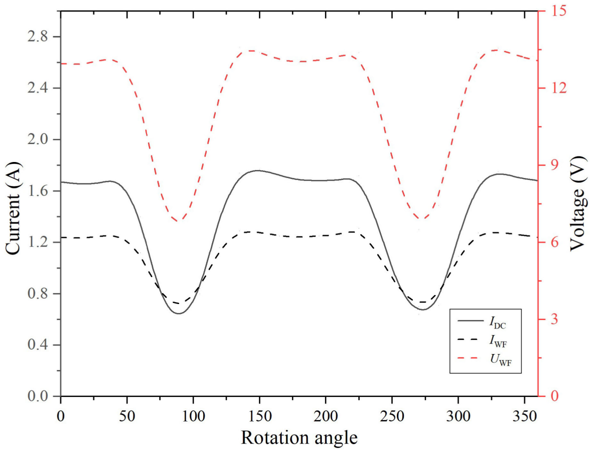

Fig. 18. I_{DC}, U_{WF}, and I_{WF} with rotation angle α changing.

12 Ω, as shown in the Fig. 18. It can be noticed that the changing trends of input current I_{DC}, output voltage U_{WF}, and output current I_{WF} are similar to that of mutual inductance. At $\alpha = 0°$, $I_{\mathrm{DC}} = 1.67$ A, $U_{\mathrm{WF}} = 12.96$ V, $I_{\mathrm{WF}} = 1.24$ A; at $\alpha = 90°$, $I_{\mathrm{DC}} = 0.58$ A, $U_{\mathrm{WF}} = 6.73$ V, and $I_{\mathrm{WF}} = 0.64$ A. To simplify the analysis, set $I_{\mathrm{DC}} = I_{P2}$, $U_{\mathrm{WF}} = U_{S2}$, and $I_{\mathrm{WF}} = I_{S2}$. In this article, I_{P2}, U_S, and I_{S2} are substituted into (5), respectively, to obtain the corresponding mutual inductance value, as shown in Fig. 19. Based on the mutual inductance mentioned above, the rotor state can be identified. It can be clearly found that the changing pattern of the mutual inductance as α changes (obtained from Fig. 19) and that of the measured mutual inductance with α changing (obtained from Fig. 15) is similar, but there is a certain difference between these mutual inductance values (in Figs. 15 and 19). This difference is caused by the inaccuracy of the mutual inductance identification model which might be caused by the neglect of the resistance of the radial-flux coupler, the internal resistance of the power supply, and the internal resistance of the inverter. However, the proposed state identification algorithm in Fig. 12 is still feasible despite this error. Thus, at $\alpha = 60°$, M_{compare} is the mutual inductance value calculated by identification model (under optimal voltage and load), which is between the mutual inductance value calculated at $\alpha = 0°$ and the mutual inductance value calculated at $\alpha = 90°$.

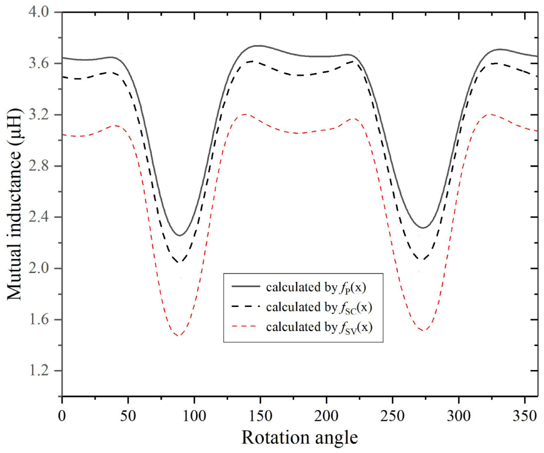

Fig. 19. Mutual inductance values obtained by $f_P(x)$, $f_{\mathrm{SC}}(x)$, and $f_{\mathrm{SV}}(x)$.

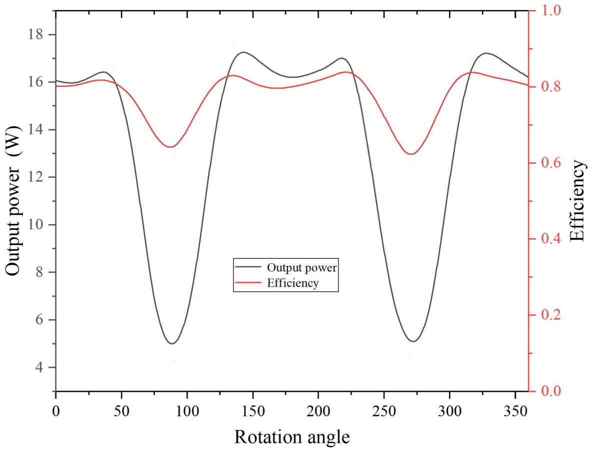

Fig. 20. Output power and efficiency versus rotation angle.

The output power and efficiency of the RF-R-WPT system with the rotation angle α changing is shown in Fig. 20. It can be known that at $\alpha = 0°$, the transmission power of the RF-R-WPT system is 16.07 W, and the transmission efficiency is 80.19%; at $\alpha = 90°$, the transmission power of the RF-R-WPT system is 4.31 W, and the transmission efficiency is 61.91%. Furthermore, the efficiency of the proposed RF-R-WPT system versus rotation angle at different offset has been measured, as shown in Fig. 21. With the increase of axial offset (from 5 to 10 mm), the comprehensive transmission efficiency decreases significantly. Reasons for this phenomenon include (but not confined to): a. a sharp decrease in the coupling coefficient of RF coupler due to the radial offset; b. the deviation of the compensation network from the optimal frequency. The increase of radial offset (from 1 to 3 mm) has little effect on the efficiency. This is because the coupling state of the RF coupler does not change much comparing with the case without offset.

The above experiments on transmission characteristics are all performed under static conditions, in which the rotor does not rotate. To obtain the motional performance of the RF-R-WPT system proposed in this article, a rotational experiment has been carried out. At 100 and 500 r/min, the input current I_{DC}, output voltage U_{WF}, and output current I_{WF} have been obtained

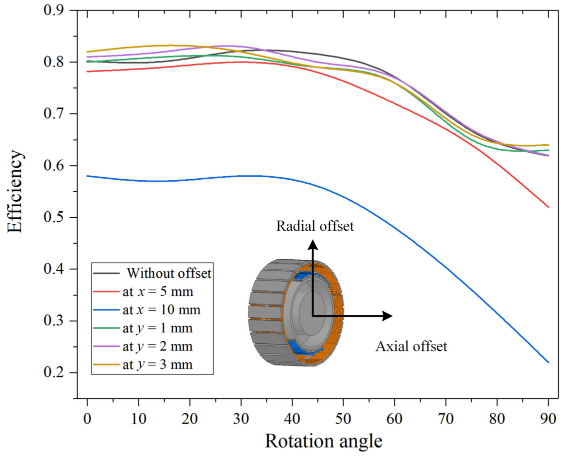

Fig. 21. Efficiency versus rotation angle at different offset (x is the axial offset; y is the radial offset).

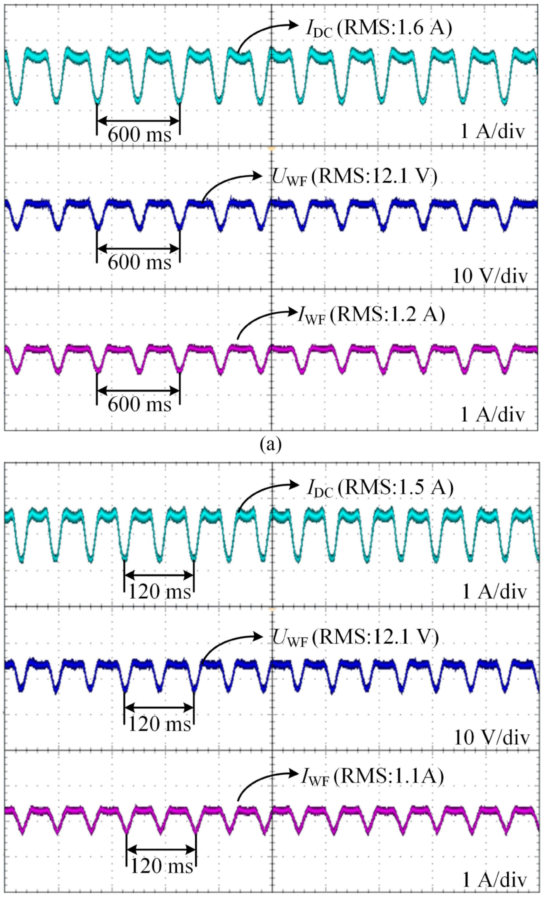

(a)

(b)

Fig. 22. $I_{\rm DC}$, $U_{\rm WF}$, and $I_{\rm WF}$ at different speeds. (a) At 100 r/min. (b) At 500 r/min.

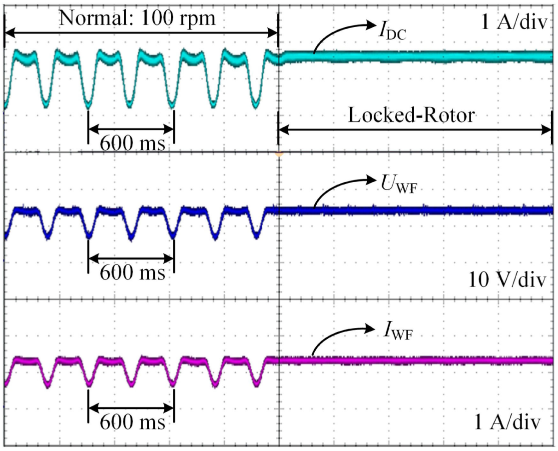

Fig. 23. $I_{\rm DC}$, $U_{\rm WF}$, and $I_{\rm WF}$ at locked rotor state.

by experiments, as shown in Fig. 22(a) and (b), respectively. It can be seen that the changing trend of input current $I_{\rm DC}$, output voltage $U_{\rm WF}$, and output current $I_{\rm WF}$ in rotating state is similar to that in stationary state. At the experimental speed of 100 r/min, twice of the $I_{\rm DC}$ variation cycle is 600 ms. According to the mutual inductance identification model $f_{\rm P}(x)$, the real-time mutual inductance can be obtained, and twice of the real-time mutual inductance variation cycle is also 600 ms. Furthermore, the speed obtained from the state recognition algorithm is the same as the experimental speed, thus it verifies the proposed theory. The integrated output power of the RF-R-WPT system is about 13.5 W, the comprehensive transmission efficiency is about 74.1% and independent of the rotation rate.

Through the locked rotor experiment, the input and output characteristics of the RF-R-WPT system have been obtained. At 100 r/min, the input current $I_{\rm DC}$, the output voltage $U_{\rm WF}$, and the output current $I_{\rm WF}$ are obtained, respectively, as shown in Fig. 23. It can be clearly recognized that when the rotor is at locked state, $I_{\rm DC}$, $U_{\rm WF}$, $I_{\rm WF}$ maintain a fixed value, which is determined by the rotation angle α.

In summary, the input and output characteristics of the RF-R-WPT system collected in the above experiment are consistent with the analysis in Section II. Experiments have confirmed that the system proposed in this article can not only supply power but also monitor the state of the rotor and determine whether the rotor is locked.

VIII. CONCLUSION

Rotational wireless power transfer technology which can transmit electric power without contact, has attracted more and more attention. A new RF-R-WPT system with state identification function has been proposed in this article. The coupler topology (including the ferrite pad), compensation topology, mutual inductance, and its identification model of the proposed RF-R-WPT system have been analyzed in this article. The prototype is built and tested. The experimental results agree well with the analyzation. Based on the results, following conclusion can be drawn.

1) The RF-R-WPT system realizes a stable power output of 13.5 W and a comprehensive efficiency of 74.1% at the speed of 100 and 500 r/min. The power and efficiency are not affected by speed at this level.
2) The coupling degree of the radial-flux coupler changes periodically with the rotation angle. The proposed system

can accurately monitor the rotation period and measure the rotation speed.

3) The RF-R-WPT system can accurately identify the locked-rotor state of the rotor through the collected voltage and current signals.

REFERENCES

[1] Q. Jiang and F. Chang, "A novel antibody population optimization based artificial immune system for rotating equipment anomaly detection," *J. Mech. Sci. Technol.*, vol. 34, pp. 3565–3574, Sep. 2020.

[2] S. Luo, A. Qiao, and Q. Tang, "A magnetic coupled rotary composite force sensor," *IEEE Sensors J.*, vol. 20, no. 2, pp. 745–751, Jan. 2020.

[3] P. Procaházka, "Electromagnetic simulator of rotating machine blades for noncontact sensor dynamic testing," *IEEE Trans. Instrum. Meas.*, vol. 67, no. 6, pp. 1506–1508, Jun. 2018.

[4] J. P. C. Smeets, L. Encica, and E. A. Lomonova, "Comparison of winding topologies in a pot core rotating transformer," in *Proc. Optim. Elect. Electron. Equip. (OPTIM) 2010 12th Int. Conf.*, 2010, pp. 103–110.

[5] N. L. Zietsman and N. Gule, "Optimal design methodology of a three phase rotary transformer for doubly fed induction generator application," in *Proc. IEEE Int. Elect. Mach. Drives Conf.*, May 2015, pp. 763–768.

[6] H. Zhong, L. Zhao, and X. Li, "Design and analysis of a three-phase rotary transformer for doubly fed induction generators," *IEEE Trans. Ind. Appl.*, vol. 51, no. 4, pp. 2791–2796, Jul. 2015.

[7] M. Ruviaro, F. Runcos, N. Sadowski, and I. M. Borges, "Analysis and test results of a brushless doubly fed induction machine with rotary transformer," *IEEE Trans. Ind. Electron.*, vol. 59, no. 6, pp. 2670–2677, Jun. 2012.

[8] Y. Meng *et al.*, "A novel wireless power transfer system with two parallel opposed coils for gastrointestinal capsule robot," *Sensors Actuators A, Phys.*, vol. 321, Apr. 2021, Art. no. 112413.

[9] C. Cai, J. Wang, H. Nie, P. Zhang, Z. Lin, and Y. Zhou, "Effective-configuration WPT systems for drones charging area extension featuring quasi-uniform magnetic coupling," *IEEE Trans. Transp. Electrific.*, vol. 6, no. 3, pp. 920–934, Sep. 2020.

[10] P. Zhang, M. Saeedifard, O. C. Onar, Q. Yang, and C. Cai, "A field enhancement integration design featuring misalignment tolerance for wireless EV charging using LCL topology," *IEEE Trans. Power Electron.*, vol. 36, no. 4, pp. 3852–3867, Apr. 2021.

[11] C. Cai *et al.*, "Improved coplanar couplers based WPT systems for adaptive energy harvesting on power towers," *IEEE Transf. Electromagn. Compat.*, vol. 63, no. 3, pp. 922–934, Jun. 2021.

[12] K. Song *et al.*, "A rotation-lightweight wireless power transfer system for solar wing driving," *IEEE Trans. Power Electron.*, vol. 34, no. 9, pp. 8816–8830, Sep. 2019.

[13] G. Lee and G. Ahn, "Wireless power transfer of daisy chain structure on rotating spindle," in *Proc. IEEE Wireless Power Transf. Conf.*, Seoul, South Korea, 2020, pp. 384–3876.

[14] A. Sofia, A. C. Tavilla, R. Gardenghi, D. Nicolis, and I. Stefanini, "Power transfer for rotating medical machine," in *Proc. 38th Annu. Int. Conf. IEEE Eng. Med. Biol. Soc.*, Orlando, FL, USA, 2016, pp. 2137–2140.

[15] J. Wang *et al.*, "Optimization design of wireless charging system for autonomous robots based on magnetic resonance coupling," *AIP Adv.*, vol. 8, 2018, Art. no. 055004.

[16] Z. Zhang, H. Pang, A. Georgiadis, and C. Cecati, "Wireless power transfer—An overview," *IEEE Trans. Ind. Electron.*, vol. 66, no. 2, pp. 1044–1058, Feb. 2019.

[17] J. Wang *et al.*, "Study of resonant self-charging rats experiment playground based on witricity technology," *Int. J. Appl. Electromagn. Mechanics*, vol. 53, no. 3, pp. 409–421, 2017.

[18] C. Cai *et al.*, "Design and optimization of load-independent magnetic resonant wireless charging system for electric vehicles," *IEEE Access*, vol. 6, pp. 17264–17274, 2018.

[19] Y. Wang, H. Wang, T. Liang, X. Zhang, D. Xu, and L. Cai, "Analysis and design of an LCC/S compensated resonant converter for inductively coupled power transfer," in *Proc. IEEE Transp. Electrific. Conf. Expo., Asia-Pacific (ITEC Asia-Pacific)*, 2017, pp. 1–5.

[20] P. Deng, B. Zhou, S. Li, X. Qing, Z. Liu, and C. Tang, "Modeling and analysis of EMI of full-bridge inverter for LCC-S compensated WPT system," in *Proc. 8th Int. Conf. Power Electron. Syst. Appl. (PESA)*, 2020, pp. 1–5.

[21] Q. Bo, Y. Zhang, Y. Guo, L. Wang, Z. Liu, and S. Li, "Sensitivity analysis to parameter variations in LCC-S compensated inductive power transfer systems," in *Proc. IEEE PELS Workshop Emerg. Technol., Wireless Power Transf. (WoW)*, 2020, pp. 233–237.

[22] J. Yang, X. Zhang, K. Zhang, X. Cui, C. Jiao, and X. Yang, "Design of LCC-S compensation topology and optimization of misalignment tolerance for inductive power transfer," *IEEE Access*, vol. 8, pp. 191309–191318, 2020.

[23] M. Budhia, J. T. Boys, G. A. Covic, and C. Huang, "Development of a single-sided flux magnetic coupler for electric vehicle IPT charging systems," *IEEE Trans. Ind. Electron.*, vol. 60, no. 1, pp. 318–328, Jan. 2013.

[24] S. Cruciani, T. Campi, F. Maradei, and M. Feliziani, "Numerical simulation of wireless power transfer system to recharge the battery of an implanted cardiac pacemaker," in *Proc. Int. Symp. Electromagn. Compat.*, 2014, pp. 44–47.

[25] Z. Dai, J. Wang, L. Jin, H. Jing, Z. Fang, and H. Hou, "A full-freedom wireless power transfer for spheroid joints," *IEEE Access*, vol. 7, pp. 18675–18684, 2019.

[26] R. L. Steigerwald, "A comparison of half-bridge resonant converter topologies," *IEEE Trans. Power Electron.*, vol. 3, no. 2, pp. 174–182, Apr. 1988.

Longyang Wang received the B.Eng. degree in 2017 from the Wuhan University of Technology, Wuhan, China, where he is currently working toward the Ph.D. degree.

His main research interests include wireless transmission technology based on magnetic resonance, linear motor, and system equipment for transmission and distribution.

Jiangui Li was born in Shanxi, China, in 1983. She received the Ph.D. degree from The University of Hong Kong, Hong Kong, in 2012.

She joined the University of Michigan as a Postdoctoral Researcher in 2012. She is currently a Professor with the School of Mechanical and Electronic Engineering, Wuhan University of Technology. Her main research topics include wireless charging, electric motor, and renewable energy power generation.

Huiying Chen was born in Hubei, China, in 1998. She received the B.Eng. degree in 2020 from the Wuhan University of Technology, Wuhan, China, where she is currently working toward the M.A. Eng. degree.

Her main research interests include wireless transmission technology based on magnetic resonance.

Zijun Pan was born in Hubei, China, in 1997. He received the B.Eng. degree in 2020 from the Wuhan University of Technology, Wuhan, China, where he is currently working toward the M.A. Eng. degree.

His main research interests include motor control and wireless power transfer.